

1 **Evaluation of TRMM 3B42 precipitation estimates and WRF retrospective**
2 **precipitation simulation over the Pacific-Andean basin of Ecuador and**
3 **Peru**

4 A. Ochoa^{1,3}, L. Pineda^{1,2}, P. Crespo³, P. Willems^{1,4}

5 ¹ KU Leuven, Department of Civil Engineering, Hydraulics Laboratory, 3001 Leuven, Belgium

6 ² Unidad de Ingeniería Civil, Geología y Minas, Universidad Técnica Particular de Loja, C/. Marcelino
7 Champagnat S/N, Loja, Ecuador

8 ³ Centro de Hidrología y Clima, Departamento de Recursos Hídricos y Ciencias Ambientales,
9 Universidad de Cuenca, Av. Víctor Manuel Albornoz, Quinta Balzaín, Cuenca, Ecuador

10 ⁴ Vrije Universiteit Brussel, Department of Hydrology and Hydraulic Engineering, 1050 Brussels,
11 Belgium

12

13 E-mail corresponding author: Luis Pineda (luis.pineda@bwk.kuleuven.be)

14 **Abstract**

15 The Pacific-Andean basin in western South-America suffers from rainfall data scarcity, as is the case
16 for many regions in the south. An important research question is whether the latest satellite-based and
17 Numerical Weather Prediction (NWP) model outputs capture well the temporal and spatial patterns of
18 rainfall over the basin, hence have the potential to compensate for the data scarcity. Based on an
19 interpolated gauge-based rainfall dataset, the performance of the Tropical Rainfall Measuring Mission
20 (TRMM) 3B42V7 and its predecessor V6, and the North Western South America Retrospective
21 Simulation (OA-NOSA30) are evaluated over 21 sub-catchments in the Pacific-Andean basin of
22 Ecuador and Peru (PAEP).

23 In general, precipitation estimates from TRMM and OA-NOSA30 capture the seasonal features of
24 precipitation in the study area. Quantitatively, only the Southern sub-catchments of Ecuador and
25 Northern Peru (3.6-6°S) are relatively well estimated by both products. The accuracy is considerably
26 less in the northern and central basins of Ecuador (0-3.6°S). It is shown that the probability of
27 detection (POD) is better for light precipitation (POD decreases from 0.6 for rates less than 5 mm day⁻¹
28 ¹ to 0.2 for rates higher than 20 mm day⁻¹). Compared to its predecessor 3B42V7 shows modest basin-
29 wide improvements in reducing biases. The improvement is specific to the coastal and open ocean
30 sub-catchments. In view of hydrological applications, the correlation of TRMM and OA-NOSA30
31 estimates with observations increases with time aggregation. The correlation is higher for the monthly
32 time aggregation in comparison with the daily, weekly and 15-daily time scales. Furthermore, it is
33 found that TRMM performs better than OA-NOSA30 in generating the spatial distribution of mean
34 annual precipitation.

35 Keywords: TRMM, WRF, KED, PAEP, Ecuador, Peru.

36 **1 Introduction**

37 Precipitation is the primary driver of the hydrologic cycle and the main input of most
38 hydrologic studies. Accurate estimation of precipitation is therefore essential. The availability
39 of rainfall data, in particular in developing countries, is hampered by the scarcity of accurate
40 high-resolution precipitation. Since its inception, rainfall measurement principles remained
41 unchanged; non-recording and recording rain gauges are still the standard equipment for
42 ground-based measuring precipitation notwithstanding that they only provide point
43 measurements. Rainfall amounts measured at different locations are traditionally extrapolated
44 to obtain areal averaged rainfall estimates. These estimates from point gauge measurements
45 will only improve, if over time the rain gauge network density increases. The latter is not
46 always the case in developing countries. In fact, in many regions gauge densities are
47 decreasing (Becker et al. 2013). One potential way to overcome the limitations of rain gauge
48 based networks and weather radar systems in estimating areal rainfall is by using satellite-
49 based global climate information and Numerical Weather Prediction (NWP) products.
50 Compared with rain gauge observations satellite rainfall data provide observations in
51 otherwise data sparse areas but their disadvantage is that they are indirect estimates of rainfall.
52 On the other hand, increased computational power and improvement of NWP models have
53 resulted into a considerable advancement in the ability to estimate rainfall. However, the main
54 limitation for NWP models is that they cannot resolve weather features that occur within a
55 single model grid box. To improve the accuracy of satellite rainfall estimation and NWP
56 models, and facilitate their intake over data sparse areas, the evaluation of both products
57 needs to be region specific and user-oriented.

58 A wide range of satellite derived precipitation products emerged the last decade and their
59 performance over different regions of the world has been evaluated. Several studies have been
60 conducted to assess the accuracy of three of the most widely used satellite based methods
61 producing global precipitation estimates, such as the Climate Prediction Centre morphing
62 method (CMORPH), Precipitation Estimation from Remotely Sensed Information Using
63 Neural Networks (PERSIANN) and the Tropical Rainfall Measuring Mission (TRMM)
64 Multisatellite Precipitation Analysis (TMPA) 3B42 (Romilly and Gebremichael, 2011).
65 TMPA 3B42V6 version performance has been evaluated over the tropical Andes of South
66 America at high-altitude regions (> 3000 m a.s.l.) by Scheel et al. (2011) with focus on the
67 Cuzco and La Paz regions in the Central Andes. Ward et al. (2011) conducted similar
68 investigation in the Paute region (> 1684 m a.s.l.) situated in the southern Ecuadorian Andes

69 and Arias-Hidalgo et al. (2013) explored its applicability as input for hydrologic studies on a
70 catchment in the Pacific-Andean basin in central Ecuador. They all concluded that
71 disregarding the limitations at small temporal scale (daily) the performance of this product
72 increases with time aggregation and highlighted the potential to use TMPA 3B42V6 at large-
73 scale basins. Dinku et al. (2010) conducted a wider evaluation covering different
74 climatological regions and altitudinal ranges of the Colombian territory. Results showed good
75 performance when the temporal scale increases (10-days), however they are region distinct
76 yielding the best performance over the eastern Colombian plain. The availability of the
77 improved version, the TMPA 3B42V7, opens a new question concerning its usefulness on
78 South-American regions. Recently, Zulkafli et al. (2014) assessed the improvement of the V7
79 over the V6 and reported a lower bias and an improved representation of the rainfall
80 distribution over the northern Peruvian Andes and the Amazon watershed. The diversity of
81 South-American environments demands new comparisons over regions with different
82 precipitation regimens and mechanisms.

83 On the other hand, NWP models capabilities keep evolving and providing precipitation fields
84 at high spatio-temporal resolutions. In general, NWP models are not only valuable tools for
85 weather forecasting but also for climate reconstruction. NWP can be initialized and bounded
86 by assimilated observational data describing the large-scale atmospheric conditions
87 throughout the reconstructed period. Periods of years to decades can be retrieved using NWP
88 models, commonly known as “regional atmospheric reanalysis”. Although, this technique is
89 still in its early stages, in tropical South America, some NWP model applications were
90 conducted by Muñoz et al. (2010). Their study follows a three-level hierarchical approach.
91 Global-scale analysis and/or GCM outputs are generated and then used as boundary
92 conditions for the meso-scale meteorological models, which in turn provide information for
93 tailored applications. In a “regional atmospheric reanalysis” setting, the Weather Research
94 and Forecasting model (WRF, Skamarock et al., 2005) was forced by applying boundary
95 conditions of the NCEP/NCAR Reanalysis project (NNRP, Kistler et al., 2001) to retrieve for
96 the first time meteorological data for North Western South America in the so-called OA-
97 NOSA30 product. The aim of the retrospective simulation was to provide input data for
98 hydrologic and health-epidemiological models with the hypothesis that the WRF retrospective
99 simulation may add skill to GCMs in countries where the Andes Mountain chain provides
100 complex disturbances that global models cannot solve.

101 The westernmost N-S axis of South America, which embraces the Pacific-Andean basin of
102 Ecuador and northern Peru (PAEP), is a region with below average density and unevenly
103 distribution of meteorological stations. Because of its location, contrasting landscapes and
104 complex topography, that includes humid regions of the western Andean foothills and arid
105 areas offshore the coastal line. The PAEP region provides a unique case to evaluate the
106 potentials and drawbacks of satellite and numerical model rainfall estimates. In consequence,
107 the objective of this study is to provide an evaluation of the performance of the TMPA V7
108 and its predecessor the TMPAV6 version and the OA-NOSA30 products versus regionalized
109 ground data over the PAEP region. Specifically, emphasis is given to determine whether there
110 are regions and time aggregation scales on which precipitation estimates may be considered
111 as an alternative and/or complementary information source for poorly gauged basins.

112

113 **2 Materials and Methods**

114

115 **2.1 Study area**

116 The western coast of South America is a region with contrasting landscapes and a rather
117 complex orography. Near to the equator the coastal area of Ecuador is drenched with rainfall
118 and supports dense vegetation down to the shore. However, at the southern margin and along
119 the northern Peruvian littoral, the coast is stark and almost devoid of vegetation. The PAEP
120 region (ca. 100800 km²) is located along the N-S axis between 0°-6°S and drains the
121 westernmost slope of the Andes Cordillera (Figure 1a). The various steep Andean ridges
122 down to the coast together with the Cordillera ‘Costanera’ shapes thirteen Pacific-Andean
123 valleys from north to south: Chone (1), Portoviejo (2), Guayas (3), Taura (4), Cañar (5),
124 Naranjal-Pagua (6), Jubones (7), Santa Rosa (8), Arenillas (9), Zarumilla (10), Puyango-
125 Tumbes (11), Catamayo-Chira (12), and Piura (13) (Figure 1b) each one with particular
126 geomorphological and climatological features. The proximity of the Andean mountain ranges
127 to the coastal line is the main influence on the basin’s relief and climatology. Short and steep
128 basins, i.e. Puyango (10), descend from nearly 4000 meters of altitude in less than 240 km of
129 river length. On the other hand, large basins host the largest plains and low land valleys in the
130 Ecuadorian littoral with roughly 70% of its area below an elevation of 200 m. The Guayas (3),
131 which is one the most important fluvial system in the western coast of South America, is such
132 large basin.

134 **2.2 Climate**

135 The coastal region of Ecuador has a seasonal rainfall distribution characterized by a single
136 rainy period, with 75-90% of the rainfall occurring between December and May. Overall, in
137 the PAEP region the rainy season starts around late November and ends in June, with a peak
138 between February and March. Over the humid Andean foothills in the coastal plain a 2-3
139 month dry period separates the rainy seasons. On top of this seasonal rainfall pattern the
140 distribution of precipitation is affected by the seasonal latitudinal migration of the Inter-
141 Tropical Convergence Zone (ITCZ) and eastern tropical Pacific Sea Surface Temperature
142 (SST) variations. The north-southern seasonal ITCZ displacement and SST variations bring to
143 the area air masses of different humidity and temperature. When the ITCZ and the equatorial
144 front are in their southernmost position near the equator, Ecuador's coastal regions are under
145 the influence of warm moist air masses, originating from the northwest, bringing significant
146 rainfall and rising air temperatures. The latter mainly defines the rainy season. Inversely, the
147 northernmost ITCZ displacement and the equatorial front result in the presence of cooler and
148 dryer air masses descending from upwelling regions in the south-west, influencing the dry
149 season (Rossel and Cadier, 2009).

150 The most important feature of the rainfall variability in the PAEP region is the occurrence of
151 inter-annual anomalies as related to the large-scale circulation phenomena such as El Niño-
152 Southern Oscillation (ENSO). The PAEP region is bounded by the limit of the strong ENSO
153 influence defined by Rossel et al. (1999) as the region where the increase in mean annual
154 precipitation is greater than 40%. Therefore, in ENSO years abrupt changes in the mean
155 annual rainfall conditions are considerable with a coefficient of variation reaching 0.40
156 (Rossel and Cadier, 2009). Such increase is not uniform basin-wide, there are important
157 regional differences in heavy rainfall formation during El Niño (EN) events (Bendix and
158 Bendix, 2006) and the EN influence on rainfall variability may change substantially in short
159 distances in the same Pacific-Andean hydrological unit (Pineda et al., 2013). Furthermore,
160 since 2000 an atypical meteorological response to EN and La Niña (LN) conditions is
161 reported over the coastal plains and the western Andean highlands (Bendix et al., 2011). All
162 this results in a very complex spatio-temporal distribution of rainfall patterns during ENSO
163 and non ENSO years. These considerations are of paramount interest when dealing with data
164 quality control of unevenly distributed rain gauges in the PAEP region.

165

166 **2.3 Data**

167 **2.3.1 Rain gauge data**

168 A ground precipitation network of 131 rain gauges with daily data (~1964-2010) in the PAEP
169 region was provided by the Ecuadorian and Peruvian Meteorological and Hydrological
170 Services, INAMHI and SENAMHI, respectively (Figure 1b). Records with gaps higher than
171 20% were excluded resulting in 107 locations with long-term daily rainfall time series.

172 In a first step, a regionalization analysis was conducted on the long-term records to group
173 spatially homogeneous stations. A station was considered as spatially homogenous if it
174 showed proportionality in the cumulative monthly volumes as referred to a control station in
175 the same sub-catchment. The most reliable records were identified by selecting records with
176 no changes in location and instrument type and then set as control stations for a double mass
177 analysis (Wilson, 1983). In the double mass analysis, the hierarchical criteria to check
178 proportionality between the control and the candidate station involves: i) neighbouring, ii)
179 similarity in altitude, and iii) exposure to the same meso/synoptic climatological feature (e.g.
180 ENSO).

181 Next, the temporal homogeneity of each record was checked against error measurements. A
182 record was considered as temporally homogenous if the record showed no step changes (shifts
183 in the means) or if the detected step changes were attributed only to climatic processes. The
184 R-based RHtests_dlyPrpc software package, developed by the Climate Research Division of
185 the Meteorological Service of Canada and which is available from the Expert Team on
186 Climate Change Detection, Monitoring and Indices (ETCCDMI) website (Wang and Feng,
187 2012), was used to identify multiple step changes at documented or undocumented change
188 points. It is based on the integration of a Box-Cox power transformation into a common trend
189 two-phase regression model suitable for non-Gaussians series such as non-zero daily
190 precipitation (Wang et al., 2010). Documented changes (EN driven) are referred as those
191 defined by Rossel and Cadier (2009) and are the sequence of at least three consecutive
192 months where the monthly SST anomalies are above 23°C and exhibit a positive anomaly
193 equal or greater than 1°C. Such events occurred in the years 1965, 1972-1973, 1976, 1982-
194 1983, 1987, 1992 and 1997-1998. For LN driven-changes the year 2008 was also considered.
195 Non-homogeneous periods were considered as modifications in the field during data

196 collection and set as Not Available (NA) and then retested to verify whether they are
197 homogeneous with the disregarded period(s).

198 **2.3.2 Gridded rainfall dataset**

199 In this study we compare basin station-gridded precipitation fields against basin averaged
200 precipitation products. Rather than rescaling the products to an arbitrary resolution the
201 products were evaluated at sub-catchment scale identified during the regionalization analysis.
202 Namely, instead of a punctual comparison, spatial averages were calculated for the
203 precipitation products using the proportional coverage of each grid cell. The analysis was
204 performed for the 1998-2008 11yr period. This period was chosen as common between the
205 TMPA products and the WRF retrospective simulation. All data-quality checked records were
206 interpolated to obtain spatial averages in each sub-catchment, except the few whose data is
207 available through the Global Telecommunication System (GTS). Data from these stations
208 may have been used for adjusting TRMM estimates. Three GTS stations were identified in
209 our dataset and excluded. The locations of the GTS stations (five) are shown in Figure 1b.

210 Using the kriging approach for spatial interpolation of daily rainfall over complex terrains, the
211 incorporation of correlation with topography/altitude has been suggested to improve
212 performance; see Buytaert et al. (2006) for highlands ~3500 m a.s.l. and Cedeño and Cornejo
213 (2008) for the coastal region below 1350 masl in Ecuador. Aslo, in a climatological study for
214 Ecuador and North Peru, Bendix and Bendix (1998) showed that the inclusion of the altitude
215 increases significantly the performance of kriging.

216 In parallel, several interpolation techniques of increasing complexity have been developed
217 and evaluated using the gstat R package (Edzer Pebesma, 2011). Inverse distance weighting
218 (IDW) and original kriging (OK) are fairly similar; both take into account the distance
219 between stations, but OK has a more complex formulation and therefore expected to be more
220 accurate. Linear regression (LR) is supposed to perform similar to kriging with external drift
221 (KED) since they both implement regression with altitude. KED is, however, more accurate
222 accounting for kriging of residuals, which means that distance between stations influences
223 interpolation as well. To discern among different interpolation techniques Li and Heap (2008)
224 recommends assessing the performance by cross validation methods.

225 A key issue in this study is whether the change of spatial support provides a sound reference
226 for comparison with TMPA's and WRF products. While the cross validation analysis
227 provides residuals variance to address uncertainty among interpolation techniques, it is

228 acknowledged that kriging variance is not a true estimate of uncertainty (Yamamoto, 2000
 229 and Haylock et al., 2008). In general, errors and uncertainty in a gridded dataset arise from
 230 many sources, including errors in the different steps of the data supply chain (measurements,
 231 collection, homogeneity) and in the interpolation technique. It would be ideal to split and
 232 quantify all of them. This is, however, not possible without the possibility to track them back.
 233 A solution would be to perform an ensemble of stochastic simulations from which uncertainty
 234 can be estimated at the expense of highly computational resources. Such detailed analysis is
 235 out of the scope of this work. We therefore quantify the total residual variance and split it up
 236 in its main contributing residual variance sources (input (data) and kriging interpolation (geo-
 237 statistical model)) based on a variance decomposition technique (Willems, 2008, 2012) in
 238 order to estimate the fraction of each contributing source. The total residual variance is
 239 assessed based on statistical analysis of the residuals between each precipitation product (Y_{PP})
 240 and KED estimates (Y_{KED}). The underlying assumption of the variance decomposition is that
 241 the (causes of the) errors on the Y_{PP} and Y_{KED} precipitation estimates are highly different,
 242 hence that they can be assumed independent. The residuals are converted into homoscedastic
 243 residuals by means of a Box-Cox (BC) transformation (Box & Cox, 1964). After this
 244 conversion, the total Y_{PP} residual variance ($S_{BC(Y_{PP,Residual})}^2$) is decomposed into the precipitation
 245 product error variance, hereafter called model error variance ($S_{BC(Y_{PP,Model})}^2$), and the KED error
 246 variance ($S_{BC(KED)}^2$) (Equation 1).

247 The KED uncertainty is evaluated using just the random field provided by a single realization
 248 with prescribed parameters (i.e. mean structure, residual variogram) (Yamamoto, 2000). We
 249 estimate the total (Y_{PP}) residual variance at every tile ($_{PP-KED}$). By subtracting the KED error
 250 variance from the total residual variance of Y_{PP} based on Equation (1), we obtain indirect
 251 estimates of the model error variance and map its spatial distribution.

$$252 \quad S_{BC(Y_{PP,Residual})}^2 = S_{BC(Y_{PP,Model})}^2 + S_{BC(KED)}^2 \quad (1)$$

253

254 **2.3.3 TMPA TRMM 3B42 products**

255 The TMPA 3B42 V7 and its predecessor version V6 version are used in this study. The
 256 TMPA 3B42V6 consists of hourly rainfall rates (mm h^{-1}) at surface level with a global
 257 coverage between 50° N and S since 1998. This method combined precipitation estimates of
 258 four passive microwave (PMW) sensors, namely TRMM Microwave Imager (TMI), Special
 259 Sensor Microwave/Imager (SSM/I) F13, F14 and F15, Advanced Microwave Scanning

260 Radiometer-EOS (AMSR-E) and Advanced Microwave Sounding Unit-B (AMSU-B). The
261 TMPA V6 algorithm is described in Huffman et al. (2007). The improved version, the 3B42
262 V7, includes consistently reprocessed versions for the data sources used in 3B42V6 and
263 introduces additional datasets, including the Special Sensor Microwave Imager/Sounder
264 (SSMIS) F16-17 and Microwave Humidity Sounder (MHS) (N18 and N19), the
265 Meteorological Operational satellite programme (MetOp) and the 0.07° Grsat-B1 infrared
266 data. The changes in the V7 algorithm at various processing levels are described in Huffman
267 et al. (2010) and Huffman and Bolvin (2012).

268 It is useful to review some of the efforts in validating TMPA V6 and/or comparing V6 and V7
269 at low and high altitudes in the tropical Pacific because it has a bearing on the choice of the
270 satellite products used in our study. While evaluating several precipitation products, Dinku et
271 al. (2010) reported that V6 outperforms other satellite products (i.e. CMORPH) at 10-daily
272 accumulation over the dry northern Colombian littoral. The converse was found over the wet
273 western Pacific coast where CMORPH was slightly better especially at daily scale. In an
274 evaluation of V7 daily rainfall estimates to analyze tropical cyclone rainfall, Cheng et al.
275 (2013) found improved skill scores over coastal and island sites in the tropical Pacific. Also,
276 Zulkafli et al. (2014) reported that the improvement of V7 against V6 is a reduction of the
277 bias especially in the Peruvian Pacific lowlands. To assess whether such improvements are
278 seen in the PAEP region, we use both TMPA versions. TMPA 3B42V6 and 3B42V7
279 precipitation estimates having 3-hourly, 0.25x0.25 degrees resolution were aggregated to
280 daily data for the 11yr period.

281

282 **2.3.4 WRF retrospective simulation**

283 The Scientific Modelling Centre from Venezuela (CMC) and the National Institute of
284 Hydrology and Meteorology from Ecuador (INAMHI) developed a North Western South
285 America Retrospective simulation. The dataset, called OA-NOSA30, is available online at the
286 International Research Institute for Climate and Society (IRI) web page (Muñoz and Recalde,
287 2010). The simulation provides numerous climate variables with a 30 km spatial and 6-hour
288 temporal resolution for the period January 1996 to December 2008 and a global coverage
289 between 11°S to 17°N and 98°W to 50°E. The accumulated precipitation was extracted on a
290 daily basis for the 11-year common period.

291 OA-NOSA30 is the simulation result from the Weather Research and Forecasting (WRF)
 292 model, a Regional Climate Model (RCM) herein used to downscale the meteorological data
 293 from the NCEP/NCAR Reanalysis Project (NNRP or R1, details at Kistler et al., 2001).
 294 NNRP stands for the combination of global climate model outputs and observations. The
 295 WRF configuration for the Microphysics Parameterization, governing the outputs, was
 296 applied. Muñoz and Recalde (2010) explained that the microphysics were modelled by the
 297 Kessler scheme (RRTM), the Dudhia schemes were used for the modelling of the longwave
 298 and shortwave radiation, respectively; the Monin-Obukhov (Janjic) scheme for modelling of
 299 the surface-layer; and the thermal diffusion with 5 soil levels for modelling the land-surface
 300 physics. Finally the Mellor-Yamada-Janjic TKE scheme was applied for describing the
 301 boundary-layer option, in which the SST update option was selected.

302

303 **2.4 Rainfall products evaluation**

304 Bias, root mean square error (RMSE) and Pearson's correlation (γ_{xy}) were applied to analyse
 305 the accuracy of the TMPA's and OA-NOSA30 estimates comparing them with rain-gauge
 306 interpolated estimates at sub-catchment scale (Equations 1 to 3). RMSE includes both
 307 systematic (bias) and non-systematic (random) errors.

$$308 \quad BIAS = \frac{1}{n} \sum_{i=1}^n (P_{xi}^{PP} - P_{xi}^{gauge}) \quad (2)$$

$$309 \quad RMSE = \sqrt{\frac{1}{n} \sum_{i=1}^n (P_{xi}^{PP} - P_{xi}^{gauge})^2} \quad (3)$$

$$310 \quad \gamma_{xy} = \frac{Cov(P^{PP}, P^{gauge})}{\sqrt{Var(P^{PP})} \times \sqrt{Var(P^{gauge})}} \quad (4)$$

311

312 Where, P^{PP} is the precipitation products value, P^{gauge} the interpolation estimate from rain
 313 gauge values, and n the number of observations.

314 Additionally, skill scores were calculated to quantify the products accuracy in detecting daily
 315 accumulation at different precipitation thresholds and they were calculated based on average
 316 sub-catchment precipitation. The Probability of Detection (POD) gives the fraction of rain
 317 occurrences that were correctly detected; it ranges from 0 to a perfect score of 1. The
 318 Equitable Threat Score (ETS) measures the fraction of observed and/or detected rain that was
 319 correctly detected and adjusted for the number of hits that could be expected due purely to
 320 random chance. A perfect score for the ETS is 1. The Frequency Bias Index (FBI) is the ratio

321 of the number of estimated to observed rain events; it can indicate whether there is a tendency
322 to underestimate or overestimate rainy events. It ranges from 0 to infinity with a perfect score
323 of 1. The False Alarm Rate (FAR) measures the fraction of rain detections that were actually
324 false alarms. It ranges from 0 to 1 with a perfect score of 0 (Su et al., 2008).

325 The ETS is commonly used as an overall skill measure by the numerical weather prediction
326 community, whereas the FBI, FAR, and POD provide complementary information about bias,
327 false alarms, and misses. To evaluate the performance of the products for light and heavy
328 precipitation events they were calculated for each sub-catchment and for several thresholds:
329 0.1, 0.5, 1, 2, 5, 10, and 20 mm day⁻¹ (Schaefer, 1990; Su et al., 2008).

330 Seasonality accuracy at sub-catchment level was evaluated confronting precipitation estimates
331 against interpolated average monthly rainfall depths. Furthermore, in order to evaluate
332 precipitation products on increasing time scales, daily, weekly, 15-daily and monthly
333 estimates were accumulated deriving Pearson's correlation (Equation 3) and relative bias. The
334 relative bias was calculated for daily/weekly/15days/monthly time aggregations by
335 normalizing the Bias (Equation 1) in order to compare different time resolutions. Finally,
336 annual mean precipitation was calculated for interpolated rain gauges and precipitation
337 products and depicted spatially.

338

339 **3 Results**

340 **3.1 Data quality verification, interpolation and uncertainty**

341 The double mass analysis discriminated 21 sub-catchments within which rainfall is spatially
342 correlated. The proportionality is strong in the coastal areas where the altitude range is narrow
343 but is less marked at higher altitudes. Four stations do not have significant correlation with
344 any other station, and the sub-catchments in which they are situated were ranked as
345 independent.

346 The temporal homogeneity check for each station reported several change-points, with a
347 statistical significance of 5%. However, most of them were attributed to EN regional
348 variations and therefore rejected as artificial change-points. Besides the documented changes,
349 several change-points appeared repeatedly in nearby locations. They were interpreted as a
350 common modification in the local climate and therefore disregarded as change-points. Despite
351 of these considerations, non-homogeneous periods significant at 5% were found in 30
352 stations. Those periods were discarded and the stations tested again for homogeneity. Nine

353 stations did not pass the test. Therefore they were no longer taken into account, resulting into
354 a quality checked set of 98 time series. From this dataset the 11yr period, January 1998 to
355 December 2008, was taken for the comparison between OA-NOSA30 and the TMPA's
356 estimates, and rain gauge precipitation data. The 98 homogeneous stations together with the
357 21 homogenous sub-catchments are shown in Figure 1b. The area and the density of the rain
358 gauge stations per sub-catchment are listed in Table 1. The highest density is found in Quiroz,
359 Upper Guayas, Alamor, Chipillico and the lowest in Naranjal-Pagua, Lower Guayas and Piura
360 and Tumbes.

361 Table 2 reports the mean cross validation results of the four investigated techniques to grid
362 daily precipitation in the period 1998-2008. Correlation for KED (0.49) is twice the value
363 than for IDW, LR, and OK techniques (0.26, 0.28, and 0.21, respectively). Not only its mean
364 is higher but correlation on almost every day was better than for any other technique. The
365 Mean Square Error (MSE) for KED is less than for LR and slightly less for OK. The
366 performance values explain how well the technique represents the variability of the
367 precipitation assessed by the squared of the residuals and it was found better for KED.
368 Overall, KED performed better in all statistics and LR was the second best. Finally, the KED
369 technique, which includes variogram analysis and the use of a 92x92m Digital Elevation
370 Model (DEM) from the Shuttle Radar Topography Mission (SRTM) as external drift, was
371 chosen to interpolate station precipitation. The result is a daily gridded dataset (4018 time
372 steps) with 92x92m resolution, which captures the horizontal and vertical gradients as well as
373 the most prominent orographic features. We first discuss the gridded dataset constraints and
374 related uncertainty when applying this dataset for comparison with the precipitation products.

375 Figure 2a, 2b and 2c present results of the uncertainty analysis for the comparison of OA-
376 NOSA30, TMPAV6 and V7 with KED estimates, based on the variance decomposition
377 technique of one-day single random realization. Figure 2a shows that the OA-NOSA30
378 estimates are subject to the largest model residual variance, which strongly correlates with the
379 high topographic precipitation gradients as seen over the inner-sierra foothills (i.e. Upper-
380 Guayas (5), Cañar (7) and Jubones (9)), and to a lesser extent over the moderate slopes of the
381 Cordillera Costanera (i.e. Chone (1)). The KED uncertainty has the highest contribution to the
382 total residual variance in these regions whereas in the remaining stations the contribution of
383 the KED uncertainty is more or less proportional to the total residual variance. In the
384 comparison of TMPAV6-V7 (Figures 2b and 2c) with KED estimates the spatial trends are
385 less evident. Correlation with elevation still takes place in the V6 analysis but the largest total

386 residual variance does not show clear distinction between middle (~500 masl) and high
387 altitudes (~3000 masl). For the V7 analysis the uncertainty mapping shows a more scattered
388 distribution with almost no spatial trends. In both the V6 and V7 cases, the KED contribution
389 to the total uncertainty remains slightly larger than the precipitation product error variance.
390 All results together suggests that when comparing precipitation products against KED
391 estimates, the TMPAV7 based product, in the first place, followed by the V6 product, offer
392 the best precipitation estimates since the precipitation uncertainty is less affected by the
393 topographic setting that provides the basis for our proposed gridded dataset. The largest
394 errors are encountered in the comparison between OA-NOSA30 and KED estimates at high
395 altitudes. This has implications to our catchment-averaged analysis. These limitations are
396 relevant for the results presented in the following sections.

397

398 **3.2 Daily verification**

399 Figure 3a, 3b, 3c shows the bias, RMSE and Pearson's correlation between precipitation
400 products and daily KED estimates accumulated over each sub-catchment unit and ranked
401 from N-S within the period 1998-2008. These statistics reveal a strong spatial variation; for
402 3B42V6 and OA-NOSA30 bias and RMSE decrease from North to South while correlation
403 increases, whereas for TMPA V7 significant bias reduction and increase in correlation seems
404 sub-catchment and precipitation regimen dependent.

405 TMPA V7 and V6 overestimate precipitation in all sub-catchments, with an average range
406 between 0 to ~2 mm day⁻¹. Conversely, OA-NOSA30 underestimates precipitation, except in
407 Quiroz (17) and Chipillico (19), the range of over/under estimation is within ~0.5 to -1.5 mm
408 day⁻¹ (Figure 3a). The RMSE ranges from 4 to 9 mm day⁻¹ for both TMPA estimates. The
409 RMSE gives more weight to the extremes because residuals are squared and they are typically
410 higher for precipitation extremes. Given that, particularly for TMPA V6, the bias is very high
411 in wet seasons RMSE values are higher for TMPA V6 estimates than for OA-NOSA30
412 (Figure 3b).

413 Figure 3c shows that the Pearson correlation is very similar between TMPA V6 and OA-
414 NOSA30 oscillating between 0.3 and 0.6 except in Arenillas (11) where OA-NOSA30's
415 detection fails. In the Northern region the highest correlation (0.5) is found at Lower/ Middle
416 Guayas (3)/(4) and the rest of the northern sub-catchments record correlations ~0.3. In the
417 Central region, average correlation is about 0.35. In the southern region, correlation

418 consistently rises to 0.5 in a large area (Catamayo-Chira and Piura catchments). TMPA V7
419 shows a very modest basin-wide improvement over TMPA V6 only with a notable correlation
420 increase on Chone (1), Upper Guayas (5), Taura (6), Jubones (9) and Zarumilla (12).

421 OA-NOSA30 presents almost no basin-wide bias on precipitation rates less than 1 mm day⁻¹.
422 For the southern sub-catchment: Alamor (15), Macará (16), Quiroz (17), Chira (18) and Piura
423 (21) this is up to 10 mm day⁻¹; over such a threshold precipitation is systematically
424 underestimated. TMPA V7 and V6 overestimate precipitation amounts smaller than 10 mm
425 day⁻¹ in sub-catchments in the central and southern regions. For lowland areas in the north this
426 threshold changes to 20 mm day⁻¹. As well as for OA-NOSA30, precipitations over 20 mm
427 day⁻¹ are systematically underestimated.

428 Figure 4a, 4b and 4c shows categorical scores POD, ETS, FBI and FAR for representative
429 sub-catchments distributed in the Northern, Central and Southern region corresponding to the
430 TMPA V7, V6 and OA-NOSA30 estimates. The four sub-catchments shown in Figure 3 were
431 chosen as representative according to their location and dominant precipitation regime. In the
432 humid northern part, Chone (1), a coastal and ocean exposed sub-catchment, and Middle
433 Guayas (4) in the inner core and greatly influenced by the continental climate divide, were
434 selected. In the Central region, Jubones (9) with a pronounced leeward effect; and Chira (18)
435 in the southern arid coast, were considered. Their indexes lead to conclusions which can also
436 describe the situation of the surrounding sub-catchments in each region. The difference
437 between scores of TMPA V7 (4a) and V6 (4b) is almost undistinguished, both estimates
438 shows a POD value of 0.6, on average, for precipitation rates less than 5 mm day⁻¹. It
439 gradually decreases to ~0.2 when the threshold is higher than 20 mm day⁻¹. A close inspection
440 reveals a marginal improvement of V7 over V6 only evident in Middle Guayas (4) at higher
441 thresholds. ETS scores, for precipitation estimates equal or lower than 5 mm day⁻¹, are on
442 average 0.25. ETS, a summary score that penalizes for hits that could occur due to
443 randomness, can be used to compare performance across regimes. A slight improvement of
444 V7 across all threshold is restricted to Chone (1). FAR and FBI increase with higher
445 thresholds. This means that overestimation exists over 1 or 2 mm day⁻¹ and false alarms are
446 then also present. In general, TMPA products detect amounts of precipitation higher than 5
447 mm day⁻¹ but it overestimates them; while amounts of precipitation less than 2 mm day⁻¹ are
448 detected with a low fraction of FAR, although bias is present. TMPA's scores are better in the
449 Southern region, Chira (1).

450 Figure 4c show the same categorical scores for OA-NOSA30. In all sub-catchment, POD
451 decreases when the threshold increases, indicating that the NWP estimates better small
452 precipitation events. POD decreases abruptly to 0 when considering thresholds of 5 and 10
453 mm day⁻¹ thresholds. The behaviour of ETS scores is the same as for POD but the average
454 scores are half the amount of POD. For small amounts of precipitation, i.e. less than 3 mm
455 day⁻¹, OA-NOSA30's POD scores are around 0.6 while ETS scores are 0.3. The FBI plot
456 shows underestimation. False alarms increase with higher thresholds with FAR values
457 typically in the range 0.2 to 0.5. There are no FAR values given for thresholds over 5- 10 mm
458 day⁻¹ since the POD of OA-NOSA30 is zero for those precipitation depths. Spatially, POD
459 and ETS show a better probability of detection in the Southern region and FBI shows lower
460 bias in that region compared to the Northern and Central regions; however FAR is lower in
461 the Northern region Middle Guayas (4).

462

463 **3.3 Monthly verification**

464 Although Figure 5a, 5b and 5c shows the mean monthly precipitation within the period 1998-
465 2008 for KED estimates against TMPA V7, V6 and OA-NOSA30 for the four selected sub-
466 catchments, the analysis below corresponds to all 21 sub-catchments. In general, Figure 5c
467 reveals that the three approaches yield comparable results for the Southern region, which
468 includes the sub-catchments Alamor (15), Macará (16), Quiroz (17), Chira (18), and
469 Chipillico (19). In most of the sub-catchments, all datasets depict well seasonality showing
470 wet conditions within the period January-May. In the Northern and Central regions, during
471 the wet season, TMPA V7 and V6 overestimate while OA-NOSA30 underestimates
472 precipitation (Figures 5a, 5b). The pattern of over- and underestimation is not that clear in all
473 datasets during the dry season. Maussion et al. (2011) showed that the WRF and TRMM well
474 estimated the precipitation distribution, but depths and positions of maxima do not match.
475 Additionally, they showed that WRF usually predicts more rainfall over larger areas,
476 notwithstanding WRF may be closer to reality than TRMM.

477 The density of rain gauges in the Catamayo-Chira catchment is higher and also the quality of
478 data is better (fewer missing gaps and change-points). This might indicate that KED estimates
479 are better for this area. However, in most of the Southern region TMPA and OA-NOSA30
480 estimates are similar to KED estimates even in the high altitude sub-catchment i.e. Quiroz
481 (17), which is not the case for the rest of the sub-catchments. Also, there are other sub-

482 catchments such as Catamayo (14) and Upper Guayas (5) where the precipitation estimates
483 are neither similar between them nor to KED estimates, despite the high quality of data. Thus,
484 KED estimates prove to be a good reference and the dependence of the interpolation
485 technique on the rain-gauge density (Table 1) as well as the error seen at high altitudes when
486 comparing OA-NOS30 and KED is not affecting substantially the analysis. This is a very
487 important issue, given that the density of rain gauges is relatively low and building up a
488 gridded rainfall dataset that is the least influenced by this fact is crucial. Notice that the
489 success of KED technique may differ for areas with lower gauge densities, which was not
490 tested in this study. TMPA's overestimation occurs for any precipitation amount when
491 aggregated per month (Figure 5); unlike daily aggregation where over-underestimation occurs
492 according to the amount of precipitation (see FBI scores in the Figures 4a and 4b).

493

494 **3.4 Verification on multi-temporal resolutions**

495 The Pearson correlation (Figure 6a) and bias (Figure 6b) were calculated on daily, weekly,
496 15-daily and monthly time scales for TMPAV7, V6 and OA-NOSA30. In general, correlation
497 increases with time scale, and is higher for monthly than 15-daily and weekly time aggregated
498 periods. Bias seems to accumulate when time aggregation increases as found for WRF in
499 other regions (Cheng and Steenburgh, 2005; Ruiz et al., 2010). The purpose of finding the
500 relative bias in the estimates is to quantify respectively the over-underestimation of the
501 precipitation depth. The relative bias is consistent with the correlation coefficient, decreasing
502 as the time aggregation increases. Although the daily bias is high in Jubones (9) (~1000% for
503 V7 and ~1200% for V6) and in Middle Guayas (4), higher for V7 than V6; on a weekly to
504 monthly scale the bias percentage decreases. The worst performance of both TMPA estimates
505 was found in Jubones, where correlation is lowest and bias percentage is highest. For OA-
506 NOSA30 that is the case for Chone (1) and Jubones (9). The results found for TMPA, i.e. that
507 correlation increases and bias reduces as time aggregation increases, are in agreement with
508 previous studies (Scheel et al., 2011; Habib et al., 2009; among others).

509 Aggregation of the mean annual rainfall was performed to compare the spatial performance of
510 the three approaches (OA-NOSA30, TMPAV6 and V7) against KED estimates in the study
511 area (Figure 7). Comparison shows that the TMPA estimates are closer to the spatial pattern
512 of the mean annual rainfall, though mean annual rainfall in the north and south-east are
513 overestimated. OA-NOSA30 presents a huge underestimation and does not reflect spatial

514 variability, except over the Southern region. Over the latter region, OA-NOSA30 bias is small
515 enough to represent a spatial pattern approaching the one based on TMPA estimates.

516 **4 Discussion**

517 Our analysis shows that both TMPA products overestimate precipitation in the 21-
518 subcatchments of the heterogeneous PAEP region. Key challenges in the estimation of
519 precipitation from satellite estimates arise from the processing scheme for MW and IR data.
520 The problem with IR data processing is that global algorithms do not consider the altitude of
521 the hydrometeor. Dinku et al. (2011) suggest that overestimation over dry areas may be
522 attributed to sub-cloud evaporation. While this mechanism may have implications on the
523 overestimation of TMPA onshore the coastal plain, especially in the arid Peruvian littoral
524 where a dry low-atmosphere is common all year-round; the attribution of TMPA
525 overestimation to sub-cloud evaporation on the middle/high altitude sub-catchments is
526 inconclusive. Bendix et al. (2006) showed that, over the Ecuadorian territory and
527 surroundings, average cloud-top height increases from W-E showing a more stratiform cloud
528 dynamics in the Pacific area and the coastal plains, and, that the western Cordillera is a true
529 division for the Pacific influence. These authors describe the seasonal spatial pattern of
530 cloud-top height distribution within December-May (wet season), possessing a well-defined
531 blocking height ($\sim 4.5 < 5.0$ km) between $0-3^{\circ}\text{S}$, but less marked southward. Given that IR
532 data processing scheme infers precipitation from the IR brightness temperature at the cloud
533 top (implicitly cloud height) it would be expected that overestimation follows the same spatial
534 pattern. However, our analysis showed that even though TMPA overestimation matches the
535 increasing W-E cloud-top gradient it does not explain the large overestimation in the Northern
536 bottom valleys (i.e. Lower Guayas and Chone catchment). The regional differences in cloud
537 properties between the Northern and Southern catchments help to explain the differences in
538 TMPA overestimation. Over the northern region $\sim 0^{\circ}$ (Quito-transect), (Bendix et al. 2006),
539 cloud frequency is substantially higher than the reduced cloudiness at $\sim 4^{\circ}\text{S}$ (Loja-transect).
540 To illustrate these differences Figure 8a, 8b, 8c show cloud density patterns using anomalies
541 of interpolated Outgoing Longwave Radiation (OLR) (Liebmann and Smith, 1996) as proxy
542 for cloudiness (negative anomalies imply increased cloudiness) during the rainy season within
543 1998-2008. During December-January (8a) symmetrical patterns of cloudiness are observed
544 over northern and southern sub-catchment, followed by increased cloudiness which
545 concentrates over the north-western edge during January February (8b). Then, cloudiness
546 exhibits a marked north-southeast gradient in April-May (8c). This suggests that in addition to

547 the error introduced by the estimation of the cloud-top, the TMPA overestimation on the
548 Northern catchments may also be influenced by frequent occurrence of low stratiform clouds
549 (typical on the coastal area) which under stable conditions are detached from precipitation
550 patterns (Bendix, et al., 2006). This high density of non-rain producing clouds would affect
551 the IR data retrieval resulting into overestimation.

552 The largest deficiencies of TMPA's estimates are encountered in separating the
553 windward/leeward effect of the Andean ridges on orographic rainfall which is particularly
554 witnessed in Jubones where the leeward effect is dominant. West of the climate divide there
555 is no typical precipitation gradient. Through blocking at the ridges and through re-
556 evaporation, rainfall of any origin affects more frequently higher elevations than valley floors
557 (Emck, 2007).

558 TMPA V7 and V6 estimates show different basin-wide skills on daily basis but they yield
559 comparable results particularly in the Southern region (3.6-6°S) in weekly to monthly time
560 aggregations. TMPA V7 shows localized skill that is higher than V6 on short-steep coastal and
561 ocean exposed sub-catchments but lower skills on large inland basins. The improvement is
562 seen in the detection capacity of light orographic precipitation on coastal ocean exposed sub-
563 catchments, where the spatial sampling seems to capture small precipitation gradients. Over
564 coastal areas the orographic enhancement is a small spatial scale event (Minder et al., 2008,
565 Cheng et al., 2013). In the inner-most sub-catchments where gradients on annual precipitation
566 may reach i.e. 700 mm / 100 m at 3400 masl (Emck, 2007) the temporal sampling of V7
567 cannot capture the rapid evolution of orographic rainfall and the overestimation is similar to
568 that of the V6 version.

569 OA-NOSA30 product only shows reasonable skills in the Southern region (3.6-6°S) where
570 amount and occurrence are relatively well represented. The greatest NWP limitations are
571 encountered in representing the fast enhancement of rain rates due to the effect of the coastal
572 mountains as premier barrier for moisture transport in short-steep coastal sub-catchments (3-
573 3.6 °S). The nearly null NWP detection capability is likely related to the unique rainfall rates
574 that occur on the ocean facing foothills of the Cordillera "Costanera". Unlike in most tropical
575 mountains where convective rainfall dominates in Southeast Ecuador
576 vigorous advection shape a monotonic increasing precipitation gradient with altitude. In the
577 core of the southern region, Emck (2007) reported that rainfall originates from an equal-
578 balance of advective-topographic (light) and convective (heavier) genesis. Such a
579 characteristic, over the Southern region, suggests that the NWP parameterization for OA-

580 NOSA30 is particularly suited to solve this type of precipitation. For the Northern regions,
581 which are more affected by the annual movement of the ITCZ, the influence of the continental
582 climate divide and the occurrence of more stratiform cloud, deep convection (likely the
583 dominant mechanism) is not emulated by the NWP model. A complete description of the
584 errors in the NWP implementation is out of the scope of this study, we therefore only
585 highlight some of the major sources. The lateral boundary conditions (reanalysis dataset) have
586 presumably a major role on the degradation of WRF product quality. The poor representation
587 of the Andes in the reanalysis model has showed to contribute to a modest simulation of
588 meteorological fields such as wind (Schafer et al., 2003). Maussion et al. (2011) found that
589 some undesired numerical effects and, eventually, inadequate input data can affect the
590 operational output of the WRF model, in particular for extreme events; probably by
591 overstressing certain physical processes. Jankov et al. (2005) found that the greatest
592 variability in rainfall estimates from the WRF model originates from changes in the choice of
593 the convective scheme, although notable impacts were observed from changes in the
594 microphysics and planetary boundary layer (PBL) schemes. However, Ruiz et al. (2010)
595 found that rainfall estimates only vary slightly among different configurations, but biases
596 increase with time aggregation. Those findings agree with previous studies (Blázquez and
597 Nuñez, 2009; Pessacg, 2008) and suggest that there is a common deficiency in the convective
598 schemes used for this model.

599

600 **5 Conclusions**

601 In general, TRMM V7, V6 and OA-NOSA30 estimates capture the most prominent seasonal
602 features of precipitation in the study area. Quantitatively, only the Southern sub-catchments of
603 Ecuador and Northern Peru are well estimated by both satellite and NWP estimates. There is
604 low accuracy of both approaches in the Northern and Central regions where TMPA V7 and
605 V6 overestimate while OA-NOSA30 systematically underestimates precipitation. The
606 improvement of V7 over V6 is not evident basin-wide. It appears that V7 detects better light
607 precipitation rates on coastal and ocean exposed basins. Inland the differences of the two
608 versions of TRMM 3B42 are almost unnoticeable. The separation of the windward/leeward
609 Andean effect on orographic precipitation appears as the main challenge for TMPA
610 algorithms. It was found that the detection probability is better for small rainfall depths (less

611 than 5 mm day⁻¹) than for high amounts of precipitation. OA-NOSA30 showed the best skills
612 in detecting a balanced advective/convective regime of precipitation in the Southern region.

613 Analysis of daily, weekly, 15-daily and monthly time series revealed that the correlation with
614 station observations increases and bias decreases with the time aggregation. Differences are
615 considerably larger for daily than weekly aggregation. The correlation and bias values are
616 similar in the Northern and Southern region but in the Central region correlation is smaller
617 and bias is higher for all time aggregations. TMPA V7, V6 and OA-NOSA30 are able to
618 capture relatively well the spatial pattern in the Southern region of the study area, but the
619 performance of both approaches reduces in the Northern and Central region. In general the
620 two TMPA versions perform better than OA-NOSA30.

621 In view of hydrological and water resources management applications, it has been
622 demonstrated that the potential intake of both satellite and NWP estimates in the PAEP region
623 differs among catchments and precipitation regimes. Our analysis has shown that both
624 approaches capture the mean spatial and temporal features of precipitation at weekly to
625 monthly accumulations over a particular region of Southern Ecuador-Northern Peru. These
626 findings are relevant for these poorly gauged regions where there is growing pool of
627 modelling work that rely on the use of satellite-based rainfall estimates as forcing data. Also
628 dynamical weather prediction becomes more frequently applied, but this prediction is still in
629 an experimental stage. However, for operational applications such as flood warning, which
630 demand high temporal resolution rainfall data, accurate depth and storm location estimates are
631 mandatory. The usefulness of both estimates is less promising.

632

633

634 **Acknowledgements**

635 L. Pineda was funded by an EMECW grant of European Commission for doctoral studies at
636 KU Leuven. A. Ochoa acknowledges VLIR-UOS for the scholarship, which enabled a study
637 stay in Belgium during which most of the presented research was conducted. Gratitude is
638 expressed to the National Services of Meteorology and Hydrology of Ecuador (R. Mejía,
639 INAMHI) and Peru (H. Yauri, SENAMHI) for making the station data available. The authors
640 thank D. Mora (PROMAS-Cuenca University) for assistance with geospatial information.

641

642 **References**

- 643 Arias-Hidalgo, M., Bhattacharya, B., Mynett, A. E., and van Griensven, A.: Experiences in
644 using the TMPA-3B42R satellite data to complement rain gauge measurements in the
645 Ecuadorian coastal foothills, *Hydrol. Earth Syst. Sci.*, 17, 2905-2915, doi:10.5194/hess-17-
646 2905-2013, 2013.
- 647 Becker, A., Finger, P., Meyer-Christoffer, A., Rudolf, B., Schamm, K., Schneider, U., and
648 Ziese, M.: A description of the global land-surface precipitation data products of the Global
649 Precipitation Climatology Centre with sample applications including centennial (trend)
650 analysis from 1901–present, *Earth Syst. Sci. Data*, 5, 71-99, doi:10.5194/essd-5-71-2013,
651 2013.
- 652 Bendix, J. and Bendix, A.: Climatological Aspects of the 1999/1993 El Niño in Ecuador,
653 *Bulletin de L'Institut Francaise d'Etudes Andines.*, 27;655–666.,
654 doi:http://lcrs.geographie.uni-
655 marburg.de/fileadmin/media_lcrs/paper_bendix/BENDIX_BIFED98.PDF, 1998.
- 656 Bendix, A. and Bendix, J.: Heavy rainfall episodes in Ecuador during El Niño events and
657 associated regional atmospheric circulation and SST patterns, *Adv. Geosci.*, 6, 43-49,
658 doi:10.5194/adgeo-6-43-2006, 2006.
- 659 Bendix, J., Rollenbeck, R., Gottlicher, D., Cermank, J.: Cloud occurrence and cloud properties
660 in Ecuador, *Climate Research*, Vol.30: 133-147, 2006.
- 661 Bendix, J., Trachte, K., Palacios, E., Rollenbeck, R., Göttlicher, D., Nauss, T., & Bendix, A.:
662 El Niño meets La Niña-Anomalous rainfall patterns in the “Traditional” El Niño region of
663 southern Ecuador. *Erdkunde*, 151-167,2011.
- 664 Blázquez, J. and Nuñez, M. N.: Sensitivity to convective parameterization in the WRF
665 regional model in southern South America., in *Ninth Int. Conf. on Southern Hemisphere*
666 *Meteorology and, Oceanography*. Melbourne, Australia., p. 6, Amer. Meteor. Soc., 2009.
- 667 Buytaert, W., Celleri, R., Willems, P., Bièvre, B. De and Wyseure, G.: Spatial and temporal
668 rainfall variability in mountainous areas: A case study from the south Ecuadorian Andes,
669 *Journal of Hydrology*, 329(3-4), 413–421, doi:10.1016/j.jhydrol.2006.02.031, 2006.
- 670 Cedeño, J. and Cornejo, M. P.: Evaluation of three precipitation products on ecuadorian coast,
671 [online] Available from:
672 http://wcrp.ipsl.jussieu.fr/Workshops/Reanalysis2008/Documents/Posters/P3-25_ea.pdf
673 (Accessed 12 April 2012), 2008.
- 674 Cheng, W. Y. Y. and Steenburgh, W. J.: Evaluation of Surface Sensible Weather Forecasts by
675 the WRF and the Eta Models over the Western United States, *Weather and Forecasting*, 20(5),
676 812–821, doi:10.1175/WAF885.1, 2005.
- 677 Chen, Y., Ebert, E. E., Walsh, K. J. E., and Davidson, N. E. : Evaluation of TRMM 3B42
678 precipitation estimates of tropical cyclone rainfall using PACRAIN data, *J. Geophys. Res.*
679 *Atmos.*, 118, 2184-2196, doi:10.1002/jgrd.50250, 2013

- 680 Dinku, T., Ruiz, F., Connor, S. J. and Ceccato, P.: Validation and Intercomparison of Satellite
681 Rainfall Estimates over Colombia, *Journal of Applied Meteorology and Climatology*, 49(5),
682 1004–1014, doi:10.1175/2009JAMC2260.1, 2010.
- 683 Dinku, T., Ceccato, P., Connor, S. J.: Challenges of satellite rainfall estimatin over 626
684 mountainous and arid parts of east Africa, *International Journal of Remote Sensing*, Vol. 30,
685 627 Issue 21, 2011.
- 686 Edzer Pebesma: CRAN - Package gstat, [online] Available from: [http://cran.r-](http://cran.r-project.org/web/packages/gstat/index.html)
687 [project.org/web/packages/gstat/index.html](http://cran.r-project.org/web/packages/gstat/index.html) (Accessed 17 July 2012), 2011.
- 688 Emck, Paul.: A climatology of South Ecuador, Unpublished PhD Thesis. Universität 631
689 Erlangen, Germany (2007)
- 690 Habib, E., Henschke, A. and Adler, R. F.: Evaluation of TMPA satellite-based research and
691 real-time rainfall estimates during six tropical-related heavy rainfall events over Louisiana,
692 USA, *Atmospheric Research*, 94(3), 373–388, doi:10.1016/j.atmosres.2009.06.015, 2009.
- 693 Haylock, M. R., Hofstra, N., Klein Tank, A. M. G., Klok, E. J., Jones, P. D. and New, M.: A
694 European daily high-resolution gridded data set of surface temperature and precipitation for
695 1950–2006, *J. Geophys. Res.*, 113, D20119, doi:10.1029/2008JD010201, 2008.
- 696 Huffman, G. J., Adler, R. F., Bolvin, D. T., Gu, G., Nelkin, E. J., Bowman, K. P., Hong, Y.,
697 Stocker, E. F. and Wolff, D. B.: The TRMM Multisatellite Precipitation Analysis (TMPA):
698 Quasi-Global, Multiyear, Combined-Sensor Precipitation Estimates at Fine Scales, *Journal of*
699 *Hydrometeorology*, 8(1), 38–55, doi:10.1175/JHM560.1, 2007.
- 700 Huffman, G. J., Adler, R.F., Bolvin, D.T. and Nelkin E.J: The TRMM multi-satellite
701 precipitation analysis (TMPA), in: *Satellite Rainfall Applications for Surface Hydrology*,
702 edited by Gebremichael, M. and Hossain, F., Springer Science, New York, USA, 2010.
- 703 Huffman, G. J., and Bolvin D. T.: TRMM and other data precipitation data set
704 documentation., 2012. (Accessed 01 December 2013)
- 705 Jankov, I., Jr., W. A. G., Segal, M., Shaw, B. and Koch, S. E.: The Impact of Different WRF
706 Model Physical Parameterizations and Their Interactions on Warm Season MCS Rainfall,
707 *Weather and Forecasting*, doi:<http://dx.doi.org/10.1175/WAF888.1>, 2005.
- 708 Kistler, R., Kalnay, E., Collins, W., Saha, S., White, G., Woollen, J., Chelliah, M., Ebisuzaki,
709 W., Kanamitsu, M., Kousky, V., Van Den Dool, H., Jenne, R. and Fiorino, M.: The NCEP-
710 NCAR 50-year reanalysis: monthly means CD-ROM and documentation, *Bulletin of the*
711 *American Meteorological Society*, 82(2), 247–267, 2001.
- 712 Li, J. and Heap, A. D.: A Review of Spatial Interpolation Methods for Environmental
713 Scientists, *Geoscience Australia*, 200, 137,
714 doi:http://www.ga.gov.au/image_cache/GA12526.pdf, 2008.
- 715 Liebmann, B., and Smith, C.A.: Description of a Complete (Interpolated) Outgoing
716 Longwave Radiation Dataset. *Bull. Amer. Meteor. Soc.*, 77, 1275-1277, 1996.

- 717 Maussion, F., Scherer, D., Finkelnburg, R., Richters, J., Yang, W. and Yao, T.: WRF
718 simulation of a precipitation event over the Tibetan Plateau, China – an assessment using
719 remote sensing and ground observations, *Hydrology and Earth System Sciences*, 15(6), 1795–
720 1817, doi:10.5194/hess-15-1795-2011, 2011.
- 721 Minder, J. R., Durran, D. R., Roe, G. H. and Anders, A. M.: The climatology of small-scale
722 orographic precipitation over the Olympic Mountains: Patterns and processes. *Q.J.R.*
723 *Meteorol. Soc.*, 134: 817–839, 2008
- 724 Muñoz, Á. G. and Recalde, C.: OA_NOSA30 dataset, [online] Available from:
725 http://iridl.ldeo.columbia.edu/SOURCES/.U_Zulia/.CMC/.OA_NOSA30/.surface/ (Accessed
726 3 May 2012), 2010.
- 727 Muñoz, A., Lopez, P., Velasquez, R., Monterrey, L., Leon, G., Ruiz, F., Recalde, C., Cadena,
728 J., Mejia, R., Paredes, M., Bazo, J., Reyes, C., Carrasco, G., Castellon, Y., Villarroel, C.,
729 Quintana, J. and Urdaneta, A.: An Environmental Watch System for the Andean countries: El
730 Observatorio Andino, *Bull. Amer. Meteor. Soc.*, 91, 1645–1652,
731 doi: <http://dx.doi.org/10.1175/2010BAMS2958.1>
- 732 Pessacg, N.: Precipitation sensitivity experiments using WRF (in Spanish), 80 pp., University
733 of Buenos Aires, Argentina., 2008.
- 734 Pineda, L., Ntegeka, V., and Willems, P.: Rainfall variability related to sea surface
735 temperature anomalies in a Pacific–Andean basin into Ecuador and Peru, *Adv. Geosci.*, 33,
736 53–62, doi:10.5194/adgeo-33-53-2013, 2013.
- 737 Romilly, T. G. and Gebremichael, M.: Evaluation of satellite rainfall estimates over Ethiopian
738 river basins, *Hydrology and Earth System Sciences*, 15, 1505–1514, doi:10.5194/hess-15-
739 1505-2011, 2011.
- 740 Rossel, F. and Cadier, E.: El Nino and prediction of anomalous monthly rainfalls in Ecuador,
741 *Hydrological Processes*, 23(22), 3253–3260, doi:10.1002/hyp.7401, 2009.
- 742 Rossel, F., Le Goulven, P. and Cadier, E.: Areal distribution of the influence of ENSO on the
743 annual rainfall in Ecuador, *Revue des Sciences de l'Eau*, v. 12(1) p, 1999.
- 744 Ruiz, J. J., Saulo, C. and Nogués-Paegle, J.: WRF Model Sensitivity to Choice of
745 Parameterization over South America: Validation against Surface Variables, *Monthly*
746 *Weather Review*, 138(8), 3342–3355, doi:10.1175/2010MWR3358.1, 2010.
- 747 Schaefer, J. T.: The Critical Success Index as an Indicator of Warning Skill, *Weather and*
748 *Forecasting*, 5(4), 570–575, doi:10.1175/1520-
749 0434(1990)005%253C0570:TCSIAA%253E2.0.CO;2, 1990.
- 750 Schafer, R., Avery, S. K., and Gage, K. S.: A comparison of VHF wind profiler observations
751 685 and the NCEP-NCAR Reanalysis over the tropical Pacific, *J. App. Meteor.*, 42, 873–889,
752 686, 2003.

753 Scheel, M. L. M., Rohrer, M., Huggel, C., Santos Villar, D., Silvestre, E. and Huffman, G. J.:
754 Evaluation of TRMM Multi-satellite Precipitation Analysis (TMPA) performance in the
755 Central Andes region and its dependency on spatial and temporal resolution, *Hydrology and*
756 *Earth System Sciences*, 15(8), 2649–2663, doi:10.5194/hess-15-2649-2011, 2011.

757 Skamarock, W. C., Klemp, J. B., Dudhia, J., Gill, D. O., Barker, D. M., Wang, W. and
758 Powers, J. G.: A Description of the Advanced Research WRF Version 2. NCAR Tech note.,
759 2005.

760 Su, F., Hong, Y. and Lettenmaier, D. P.: Evaluation of TRMM Multisatellite Precipitation
761 Analysis (TMPA) and Its Utility in Hydrologic Prediction in the La Plata Basin, *Journal of*
762 *Hydrometeorology*, 9(4), 622–640, doi:10.1175/2007JHM944.1, 2008.

763 Wang, X., Chen, H. and Wu, Y.: New techniques for the detection and adjustment of shifts in
764 daily precipitation data series, *Journal of Applied Meteorology and Climatology*, 49, 2416–
765 2436, doi:http://dx.doi.org/10.1175/2010JAMC2376.1, 2010.

766 Wang, X. L. and Feng, Y.: Software for detection and adjustment of shifts in daily
767 precipitation data series, [online] Available from:
768 <http://etccdi.pacificclimate.org/software.shtml>, 2012.

769 Ward, E., Buytaert, W., Peaver, L. and Wheeler, H.: Evaluation of precipitation products over
770 complex mountainous terrain: A water resources perspective, *Advances in Water Resources*,
771 34, 1222–1231, doi:10.1016/j.advwatres.2011.05.007, 2011.

772 Willems, P.: Quantification and relative comparison of different types of uncertainties in
773 sewer water quality modelling, *Water Research*, 42, 3539-3551, 2008.

774 Willems, P.: Model uncertainty analysis by variance decomposition, *Physics and Chemistry*
775 *of the Earth*, 42-44, 21-30, 2012.

776 Wilson, E. M.: *Engineering Hydrology*, 3rd ed., Macmillan., 1983.

777 Yamamoto, J. K.: An alternative measure of the reliability of ordinary kriging estimates,
778 *Math. Geol.*, 32, 489–509, doi:10.1023/A:1007577916868, 2000.

779
780 Zulkafli, Z., Buytaert, W., Onof, C., Manz, B., Tarnavsky, E., Lavado, W., and Guyot, J.: A
781 comparative performance analysis of TRMM 3B42 (TMPA) versions 6 and 7 for hydrological
782 applications over Andean-Amazon river basins, *J. Hydrometeor.*, 15,581-592,
783 doi:10.1175/JHM-D-13-094.1, 2014.

784
785
786
787

788 Table 1. Description of sub-catchments and rain gauge density of homogeneous stations

Code	Sub-catchments	Catchment	Altitudinal range (m)	Area (km ²)	Stations density*
1	Chone	Chone	0 - 350	3259	0.80
2	Portoviejo	Portoviejo	0 - 600	3548	1.00
3	Lower Guayas	Guayas	0 - 680	14641	0.30
4	Middle Guayas		0 - 4100	21423	0.70
5	Upper Guayas		300 - 4000	3642	2.50
6	Taura	Taura	0 - 2600	2449	0.40
7	Cañar	Cañar	0 - 4300	2412	1.50
8	Naranjal-Pagua	Naranjal-Pagua	0 - 4000	3387	0.01
9	Jubones	Jubones	0 - 4000	4361	1.20
10	Santa Rosa	Santa Rosa	0 - 2200	1062	0.80
11	Arenillas	Arenillas	0 - 1400	653	1.40
12	Zarumilla	Zarumilla	0 - 800	810	1.10
13	Puyango	Puyango - Tumbes	300 - 3500	3662	0.50
14	Catamayo	Catamayo - Chira	300 - 3500	4173	1.70
15	Alamor		200 - 2300	1182	2.30
16	Macará		150 - 3600	3166	2.00
17	Quiroz		150 - 3500	3137	3.70
18	Chira		0 - 800	4931	0.70
19	Chipillico		100 - 3200	1179	2.30
20	Tumbes	Puyango - Tumbes	0 - 1200	8200	0.30
21	Piura	Piura	0 - 2500	9472	0.30
Total				100745	

* Stations per precipitation products grid cell (~900 km²)

789

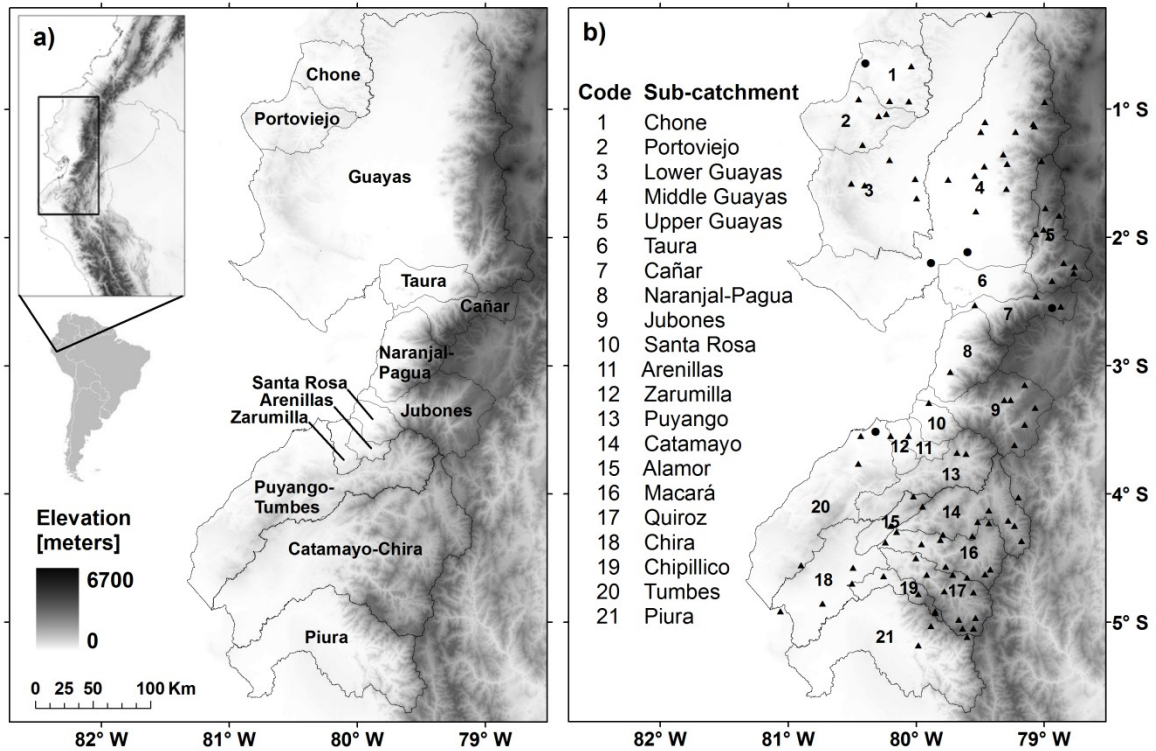
790 Table 2. Cross-validation results of daily rainfall interpolation for all stations over the period
791 1998-2008 using inverse distance weighting (IDW), linear regression with altitude (LR),
792 ordinary kriging (OK), and kriging with external drift (KED) techniques

Method	Correlation	MSE	Performance
IDW	0.260	65.33	0.012
LR	0.275	0.656	0.881
OK	0.210	0.550	0.865
KED	0.484	0.510	0.885

793

794

795



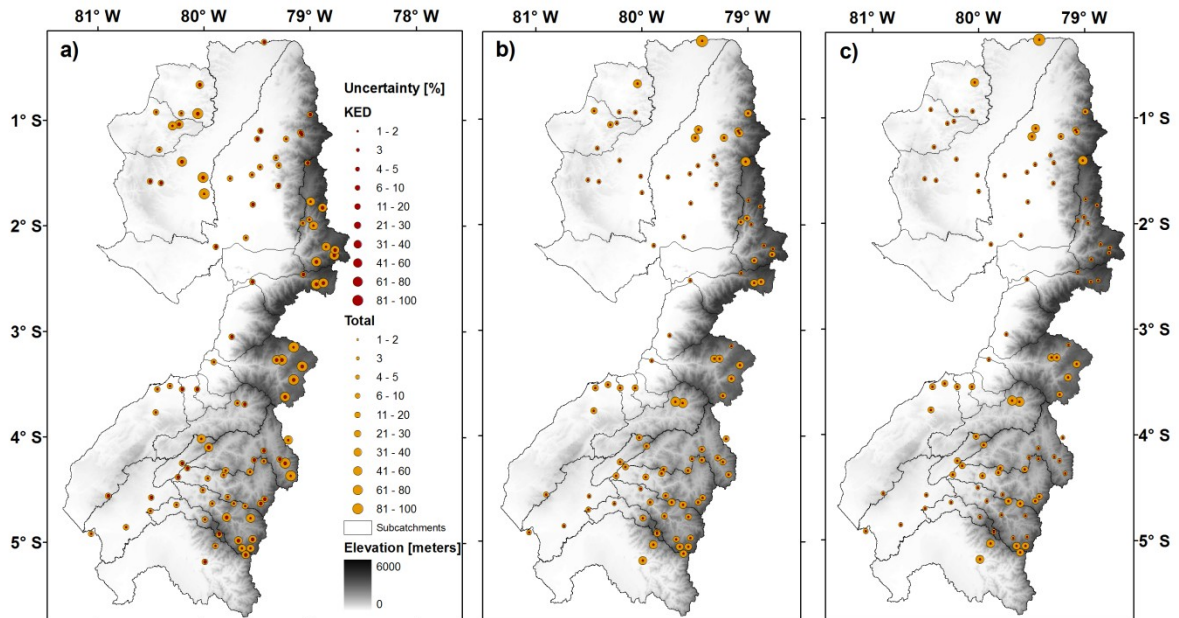
796

797

798

799

Figure 1. (a) Location of the study area. Topography and boundaries of the catchments (grey line) in the Pacific-Andean basin of Ecuador and Peru. (b) Sub-catchment boundaries (grey line) and rain gauge stations (triangles) used for the evaluation. Dots indicate GTS stations.



800

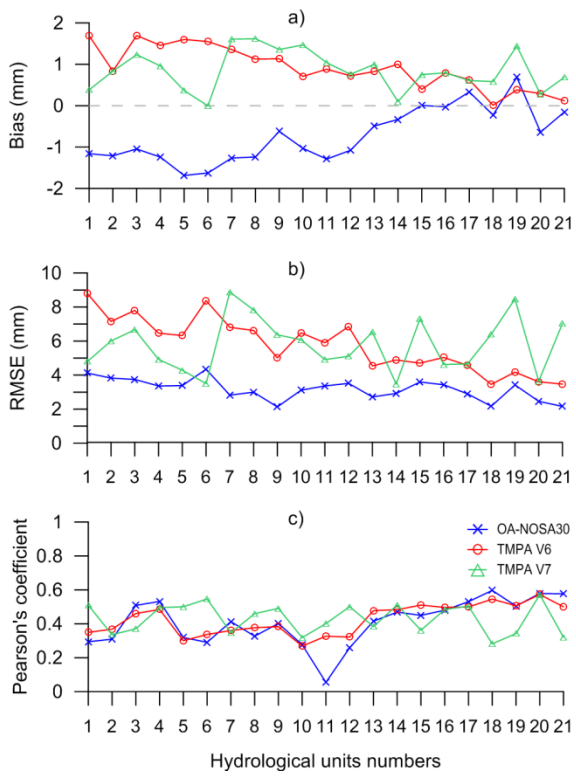
801

802

803

804

Figure 2. Spatial distribution of the total residual variance (graded orange circles) and the fractional contribution of the KED uncertainty in the total residual variance (graded red circles) based on the comparison of one-single day random KED simulation against (a) OANOSA-30, (b) TMPA V6 and (c) TMPA V7. The size of the circles is proportional to the variance value.



805

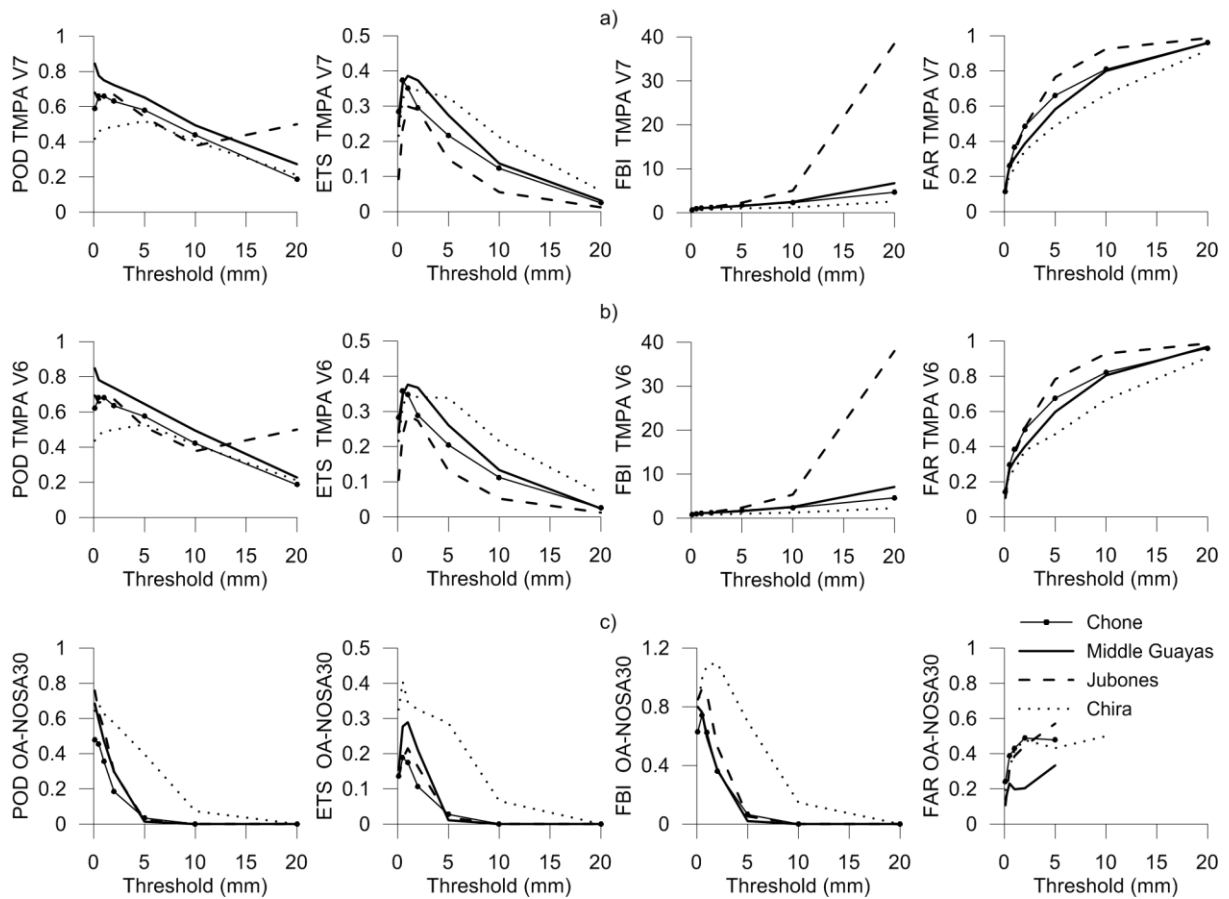
806

807

808

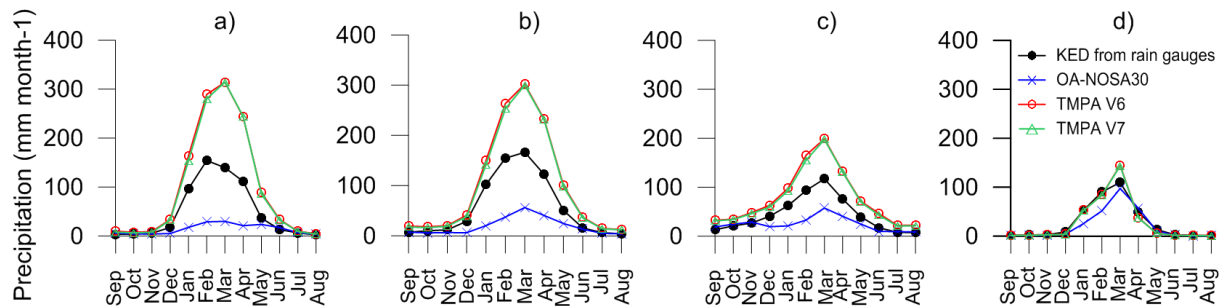
809

Figure 3. Overall performance of the daily analysis for TMPA V7, V6 and OA-NOSA30 and precipitation estimates per sub-catchment, averaged over the period 1998-2008. Names of sub-catchments corresponding to the numbers are detailed in Table 1. a) Bias b) RMSE and c) Pearson's correlation coefficient.



810
811

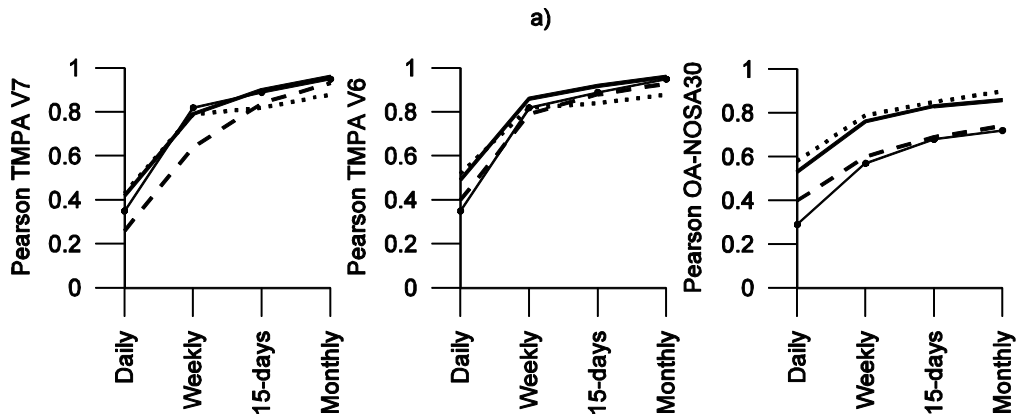
812 Figure 4. Categorical scores (POD, ETS, FBI, and FAR) of daily rainfall average for a) TMPA V7, b)
813 V6 and c) OA-NOSA30 outputs against KED interpolated station data averaged over the period 1998-
814 2008, applying different thresholds as precipitation upper limit.



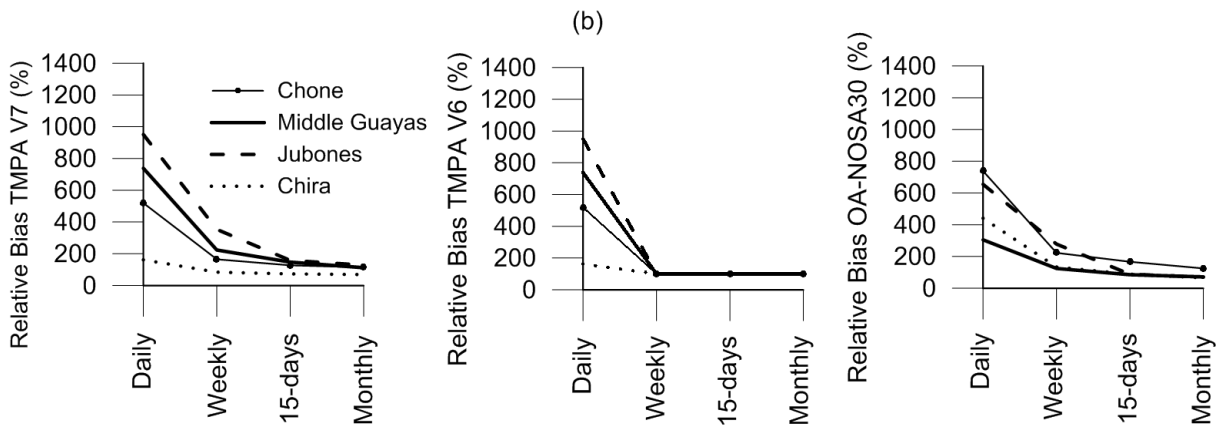
815

816 Figure 5. Mean monthly precipitation in sub-catchments from North to South: (a) Chone, (b) Middle
817 Guayas, (c) Jubones, and (d) Chira over the period 1998-2008.

818

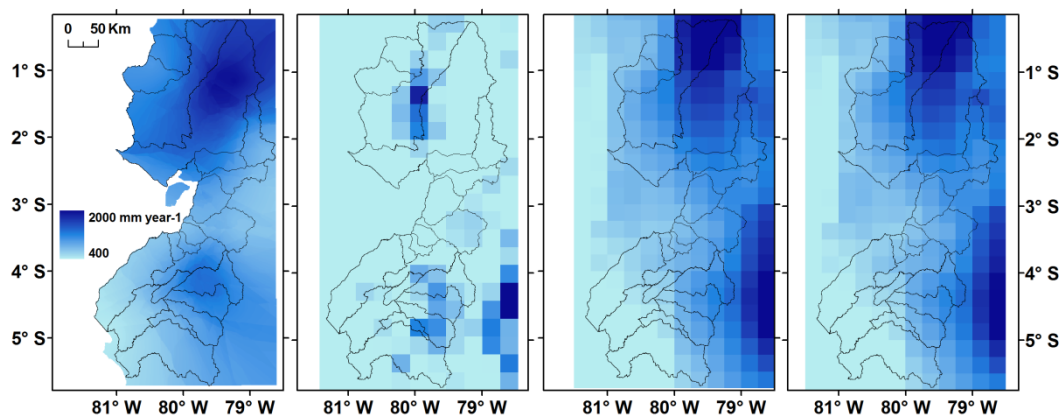


819

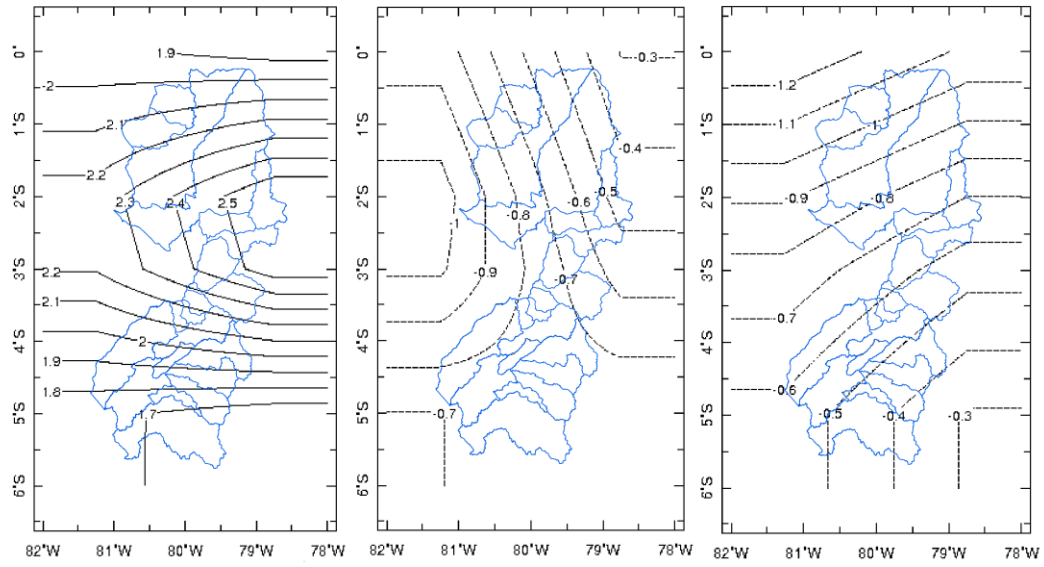


820 Figure 6. Overall performance analysis considered for daily, weekly, 15-daily and monthly time
821 aggregations over the period 1998-2008. a) Pearson's correlation coefficient and b) relative bias (%)
822 for TMPA V7, V6 and OANOSA-30 products calculated for a representative sub-catchment in the
823 north, centre and south.

824



825 Figure 7. Spatial distribution of mean annual precipitation over the period 1998-2008 according to the
826 KED interpolation of 98 rain gauges (a), OANOSA30 (b), TMPA V6 (c) and TMPA V7 (d).



827
 828 Figure 8. Monthly anomalies of OLR (Watts/m^2) during 1998-2008 within the rainy season
 829 December-January (left), February-March (centre), April-May (right).
 830
 831